Available online at www.sciencedirect.com
ScienceDirect
Journal of Sound and Vibration 302 (2007) 117–137
JOURNAL OF SOUND AND VIBRATION
www.elsevier.com/locate/jsvi

Local coupling between actuator and sensor pairs in light honeycomb structures

Chinsuk Hong*, Stephen J. Elliott

Institute of Sound and Vibration, University of Southampton, Highfield, Southampton SO17 1BJ, UK

Received 7 February 2006; received in revised form 11 September 2006; accepted 15 November 2006
Available online 12 January 2007

Abstract

This paper considers the local dynamic coupling between closely spaced actuator–sensor pairs mounted on a light honeycomb structure, with an accelerometer as a sensor and either force or piezoceramic actuator. This initial work is carried out on a resiliently mounted honeycomb beam structure and it is found that the compliance of the honeycomb core significantly affects the coupling if the actuator and sensor are closely located on opposite sides of the beam. The experimentally observed local dynamic coupling is modelled by a single-degree-of-freedom mass–spring–damper system. The effect of this coupling on the stability and performance of a direct velocity feedback control system is examined, and is shown to provide an inherently stabilising mechanism when using a piezoceramic actuator.

1. Introduction

The control of vibration in honeycomb structures is important in a number of applications, particularly the reduction of interior noise in aircraft by reducing the vibration of trim panels. Trim panels are typically light honeycomb structures, but have complicated shapes. In order to begin investigating the active control of such structures, this paper considers the coupling between closely located pairs of actuators and sensors, which may be used to implement local feedback loops, on simple honeycomb beam structures. The sensor is assumed to be a conventional accelerometer, whose output can be integrated to give the velocity signal which is fed back to the actuator. Both force actuators and piezoceramic actuators are considered since the former is an idealisation that should provide an unconditionally stable control system [1,2] and the later can be integrated into a structure and may provide a way of practically achieving multiple local control loops on practical structures [3,4].

When implementing an active control system for a honeycomb structure, the effects of the masses due to sensors and actuators of the control system must be accounted for, since their mass is comparable to that of the honeycomb structure. Furthermore, when the sensors are located on the one of the skins of the honeycomb structure, and the actuators are located on the other skin, the two masses are coupled dynamically due to the finite stiffness of the core shell in the vertical direction [5]. A similar situation can be found in the analysis of

*Corresponding author. Tel.: +44 2380 594932; fax: +44 2380 593190.
E-mail addresses: csh@isvr.soton.ac.uk (C. Hong), sje@isvr.soton.ac.uk (S.J. Elliott).

0022-460X/$ - see front matter © 2006 Elsevier Ltd. All rights reserved.
doi:10.1016/j.jsv.2006.11.006

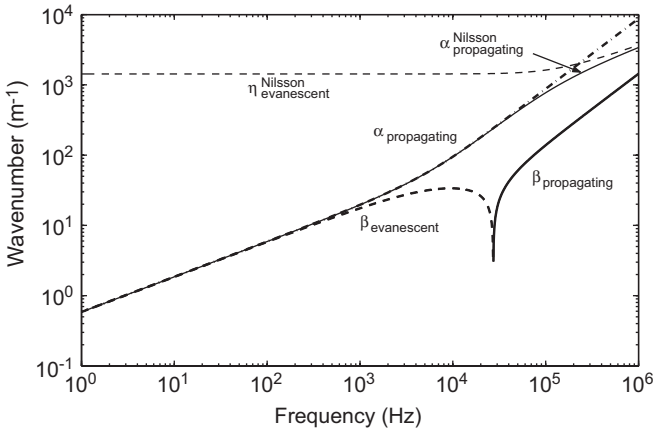

Fig. 1. Typical wave dispersion curves for honeycomb beams as predicted using the model of Nilsson [13] ($\alpha^{\text{Nilsson}}_{\text{propagating}}$, $\beta_{\text{propagating}}$, $\beta_{\text{evanescent}}$ and $\eta^{\text{Nilsson}}_{\text{propagating}}$) and those as predicted using an equivalent Timoshenko beam model ($\alpha_{\text{propagating}}$, $\beta_{\text{propagating}}$ and $\beta_{\text{evanescent}}$).

sandwich beams with honeycomb truss core [6], or truss-like beams [7,8]. The response of these structures can be divided into two frequency zones. In the low-frequency range, honeycomb beams can be modelled as an equivalent homogeneous beams using the composite material theories [9], the structural mechanics of the unit cell elements of the honeycomb structure [10,11], or by energy considerations [12]. This frequency range is limited by the existence of lumped masses and stiffnesses on the honeycomb structure and by the existence of the intracell resonances when the frequency is quite high such that the wavelengths become the order of the length of the core. Above these frequencies, the equivalence of the honeycomb core as a homogeneous structure fails, and the behaviours of the intracells must be modelled, using the transfer matrix method [7,8] and the spectral element method [6] for example.

However, in this paper we investigate the dynamic coupling that can occur at low frequencies, due to the masses and stiffness of the sensors/actuators. Nilsson et al. [13] modelled a honeycomb beam as a tightly bonded three-layered beam consisting of the two skins and honeycomb core. Fig. 1 shows the dispersion curves of a typical honeycomb structure. In additional to the waves from the classical Timoshenko beam model, a near-field wave is predicted, denoted by the faint dashed line in Fig. 1 as predicted by Nilsson. At lower frequencies the wavenumber of the near-field wave, η, is independent of frequency, indicating that it describes the local static deflection of the skin. The local static deflection is due to the stiffness of the honeycomb structure in the thickness direction. This stiffness gives rise to the dynamic coupling of the sensor–actuator pairs.

In this paper, this local dynamic coupling is investigated experimentally and theoretically on a honeycomb beam structure. It is found to provide an inherent stabilising mechanism for direct velocity feedback control systems when using the piezoelectric actuators.

2. Dynamics of a honeycomb beam

2.1. Equation of motion

Using first-order shear deformation theory (FSDT) [9,14], leading to an equivalent homogeneous beam model in the low-frequency regime, the equation of motion of a honeycomb beam can be obtained as

$$\frac{\partial}{\partial x}\left[KA_{55}\left(\frac{\partial w_0}{\partial x}+\phi_x\right)\right]+q(x,t)=I_0\frac{\partial^2 w_0}{\partial t^2}, \tag{1}$$

$$\frac{\partial}{\partial x}\left(D_{11}\frac{\partial \phi_x}{\partial x}\right)-KA_{55}\left(\frac{\partial w_0}{\partial x}+\phi_x\right)+T(x,t)=I_2\frac{\partial^2 \phi_x}{\partial t^2}, \tag{2}$$

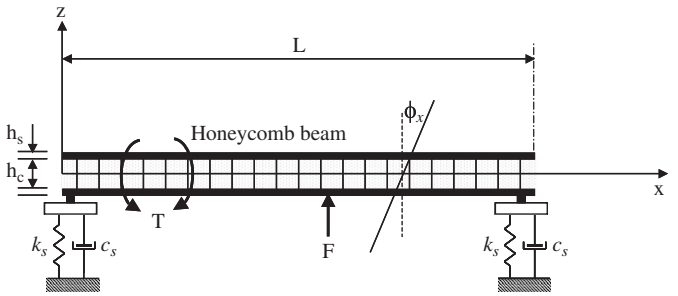

Fig. 2. Configuration of honeycomb beams where L, h_c, and h_s are the length of the honeycomb beam, the height of the honeycomb core, and thickness of the skin. The width of the honeycomb beam is to be b. ϕ_x is the rotation angle of the cross-section.

where w_0 and ϕ_x are the transverse displacement of the mid-surface of the beam and the rotational angle of the cross-section of the beam. Also, $T(x,t)$ and $q(x,t)$ are the applied moment and force per unit length as shown in Fig. 2. K is the shear correction factor which is assumed to be $K = 5/6$ for a rectangular section. The stiffness A_{55} in Eqs. (1) and (2) can be evaluated as

$$A_{55} = 2G_{xz}^{(s)}h_s + G_{xz}^{(c)}h_c \simeq G_{xz}^{(c)}h_c, \tag{3}$$

where $G_{xz}^{(s)}$ and $G_{xz}^{(c)}$ are the shear modulus of the skin and core, respectively, and h_s and h_c are the thickness of core and skin, respectively. Also, the mass density, I_0, and the rotary inertia, I_2 can be obtained as

$$I_0 = \rho^{(c)}h_c + 2\rho^{(s)}h_s, \tag{4}$$

$$I_2 = \rho^{(c)}\frac{h_c^3}{12} + \rho^{(s)}\left(\frac{h_c^2 h_s}{12} + h_c h_s^2 + \frac{2h_s^3}{3}\right), \tag{5}$$

where $\rho^{(c)}$ and $\rho^{(s)}$ are densities of core and skin, respectively. The stiffness, D_{11}, can be evaluated as

$$\begin{aligned} D_{11} &= E_{xx}^{(c)}\frac{h_c^3}{12} + E_{xx}^{(s)}\left(\frac{h_c^2 h_s}{2} + h_c h_s^2 + \frac{2h_s^3}{3}\right) \\ &\simeq E_{xx}^{(s)}\left(\frac{h_c^2 h_s}{2} + h_c h_s^2 + \frac{2h_s^3}{3}\right) \equiv E_{xx}^{(s)}I_{yy}^{(s)}/b, \end{aligned} \tag{6}$$

where the superscript (s) indicates the properties for the skins and (c) for the core, b is the width of the beam, and $I_{yy}^{(s)}$ is the cross-sectional second moment of inertia of the skin with respect to the mid-surface.

The beam is assumed to be resiliently mounted. The boundary conditions can be obtained from the force and moment equilibrium at $x = 0$ and L [15], so that, at $x = 0$

$$V = KA_{55}\left(\frac{\partial w}{\partial x} + \phi_x\right) = -k_s w - c_s\dot{w}, \quad M = D_{11}\frac{\partial \phi_x}{\partial x} = 0 \tag{7}$$

and at $x = L$

$$V = KA_{55}\left(\frac{\partial w}{\partial x} + \phi_x\right) = k_s w + c_s\dot{w}, \quad M = D_{11}\frac{\partial \phi_x}{\partial x} = 0, \tag{8}$$

where V and M are the shear force and the bending moment per unit width, and k_s and c_s are the spring constant and the damping coefficient of the mounts.

The response of the honeycomb beam to a concentrated force at x_f and a concentrated moment at x_T can be expressed as

$$w(x,t) = \sum_{m=1}^{\infty}\left[\frac{e^{j\omega_m t}}{(\omega_m^2 + 2j\zeta_m\omega\omega_m - \omega^2)}\{fW_m(x_f) + T\Phi_m(x_T)\}W_m(x)\right] \tag{9}$$

and

$$\phi(x,t)=\sum_{m=1}^{\infty}\left[\frac{e^{j\omega_m t}}{(\omega_m^2+2j\zeta_m\omega\omega_m-\omega^2)}\{fW_m(x_f)+T\Phi_m(x_T)\}\Phi_m(x)\right], \tag{10}$$

where ζ_m is the modal damping term added to take into account the structural damping, and $W_m(x)$ and $\Phi_m(x)$ are modal functions for the lateral and angular displacements, evaluated in Appendix A.

3. Experimental observation of local actuator/sensor coupling

In this section, the dynamic coupling of the actuator–sensor pair in honeycomb structure is investigated experimentally. The geometrical data of the honeycomb beam are listed in Table 1. Its mechanical properties are estimated using the procedure given in Ref. [13]. The response functions are obtained between the actuation, either force or moment pair, and the velocity measured by either an accelerometer or laser vibrometer with and without local mass as shown in Fig. 3. The arrangements take into account the type of the actuator, the mass of the sensor and the location of the mass loading. A massless sensor is accomplished by using the laser vibrometer (PSV-300). The dummy mass whose weight, 2.5 g, is the same as that of the accelerometer used is to see the effect of the local mass. The force actuator, LDS V101, is fixed on a hard and rigid test bed to improve signal-to-noise ratio, exciting the beam. The piezoceramic actuator having the size of 13 mm × 13 mm and weight of 3 g is bonded tightly on the skin of the honeycomb structure.

Fig. 4 shows the measured response functions for the force actuator–sensor pair arrangements shown in Fig. 3(a). Distinct bending modes appear at low frequencies below 2 kHz, and their phase characteristics are always between the ±90° for the configuration in which the laser vibrometer is used. It can be seen that the response function between the force applied on one side and the velocity measured with an accelerometer on the other side has strong coupling behaviour at about 4.5 kHz. At this frequency, the phase of the frequency response is shifted by ±180°, and the magnitude decreases at the rate of 12 dB/oct. Comparing the response functions from configuration F02 and F03, it is found that this does not occur if the lumped mass is on the same side of the honeycomb as the applied force.

To explore the characteristics of the local coupling further, the response functions were measured under different conditions; changing boundary conditions, the length of the beam and the mass of the sensor. The arrangement for clamping the beam at $0.4L$ and $0.6L$ and doubling the mass of the sensor is shown in Fig. 5. The response functions under six different conditions, together with free–free beam of length L, are compared in Fig. 6. In high frequencies, only the mass of the sensor affects to the broad peak due to the coupling in the mobility function, decreasing the resonance frequency. When the mass is doubled, the resonance frequency does not, however, decrease by the factor of $\sqrt{2}$, which means that the local coupling mechanism interacts with the dynamics of honeycomb beam. Since the beam length and the boundary condition do not influence the high-frequency response, it is an evidence that the response at high frequencies is dominated by the local dynamics of the actuator–sensor pair.

Table 1
Geometry and material parameters of the honeycomb beam

Parameters	Symbol	Unit	Values
Length	L	m	0.51
Width	b	m	0.04
Thickness of skin	h_s	mm	0.5
Thickness of core	h_c	mm	3
Density of skin	$\rho^{(s)}$	kg/m^3	507
Density of core	$\rho^{(c)}$	kg/m^3	169
Shear modulus of core	$G_{zx}^{(c)}$	MPa	13.7
Young's modulus of skin	$E_{xx}^{(s)}$	GPa	14.8

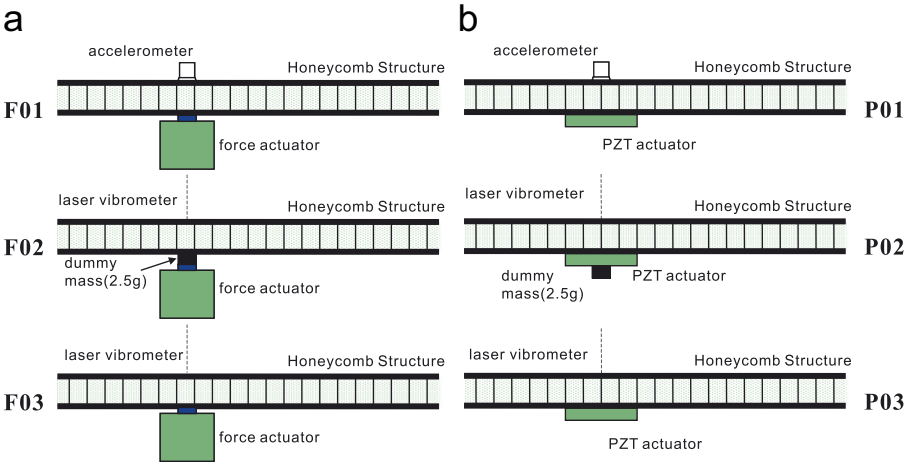

Fig. 3. Actuator–sensor pair configuration: (a) force actuator and (b) piezoceramic.

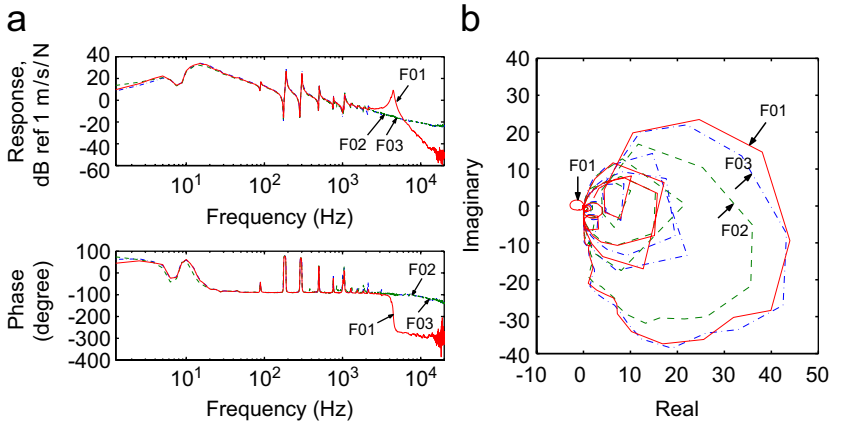

Fig. 4. Measured frequency responses using force actuators with configuration F01 (solid line), F02 (dashed line) and F03 (dot-dashed line) shown in Fig. 3(a): (a) bode diagram and (b) Nyquist plot.

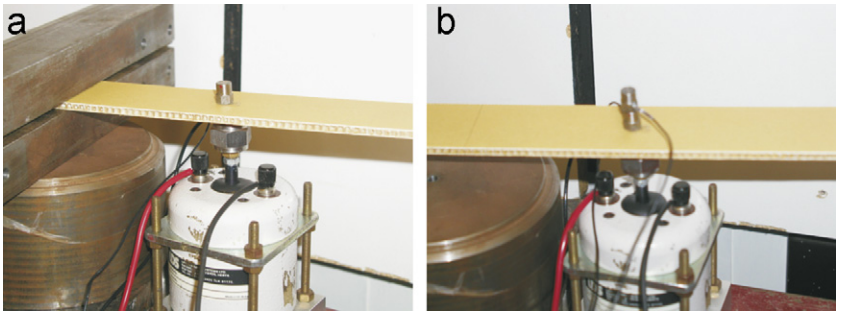

Fig. 5. Measurement of the frequency responses using the force actuator under the different conditions: (a) clamped honeycomb beam and (b) doubling the sensor's mass.

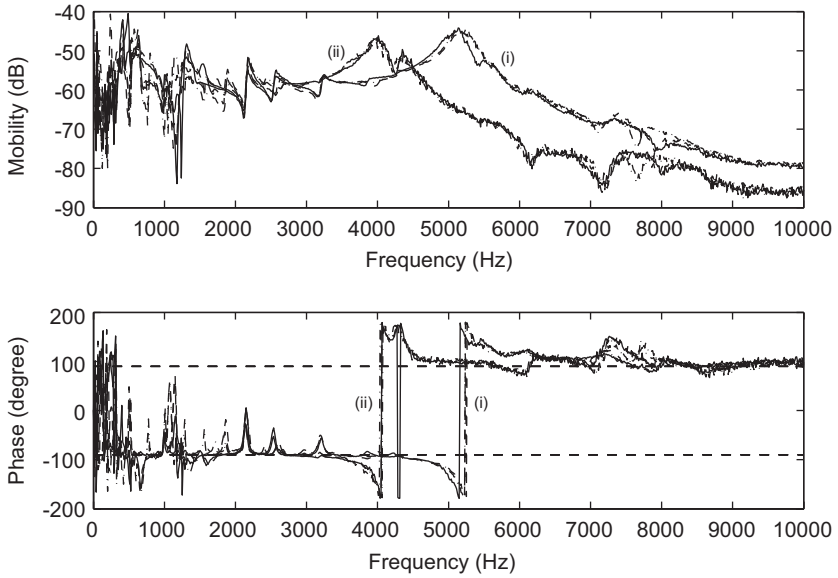

Fig. 6. Effect of the length of the beam, the boundary condition and the mass of the sensor on the plant response, when measuring it with the force applied on one side and the velocity measured at the same point on the other side. The set of curves (i) is for honeycomb beams having an accelerometer mass of 2.5 g and (ii) is for the same beams having an accelerometer mass of 5.0 g.

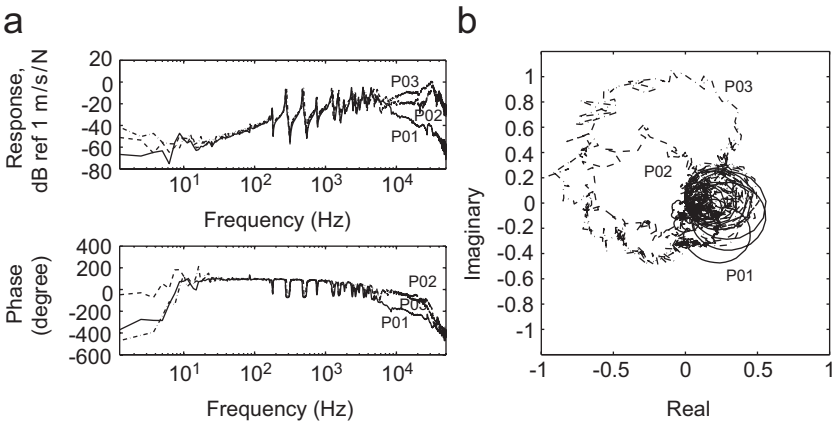

Fig. 7. Measured frequency responses using piezoceramic actuators with configuration P01 (solid line), P02 (dashed line) and P03 (dot-dashed line) shown in Fig. 3(b): (a) bode diagram and (b) Nyquist plot.

Fig. 7 shows the measured response functions of the honeycomb beam from a piezoceramic actuator attached to one side of the honeycomb beam and the velocity measured at the centre of the piezoceramic on the other side under the different configuration of lumped mass shown in Fig. 3(b). The distinct bending modes can also be found at low frequencies with their phase between the $\pm 90^\circ$, as in the case of the force actuation, but the bending modes are predominant up to 5 kHz. There does not appear to be a peak in the response due to the local dynamics in higher frequency range in this case. However, it can be seen that the response functions in the higher frequencies for the three arrangements, shown in Fig. 3(b), are quite different. The response of the beam without the lumped mass measured by the laser vibrometer increases up to 30 kHz and then decreases showing a peak. This peak is considered to be the effect of the in-plane resonance of the piezoceramic patch. This peak can be seen from the response of the beam with the lumped mass located on the

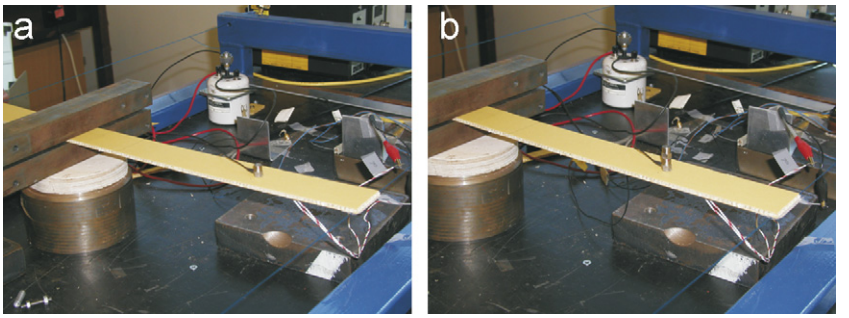

Fig. 8. Measurement of the frequency responses using piezoceramic actuator under the different conditions: (a) clamped honeycomb beam and (b) doubling sensor's mass.

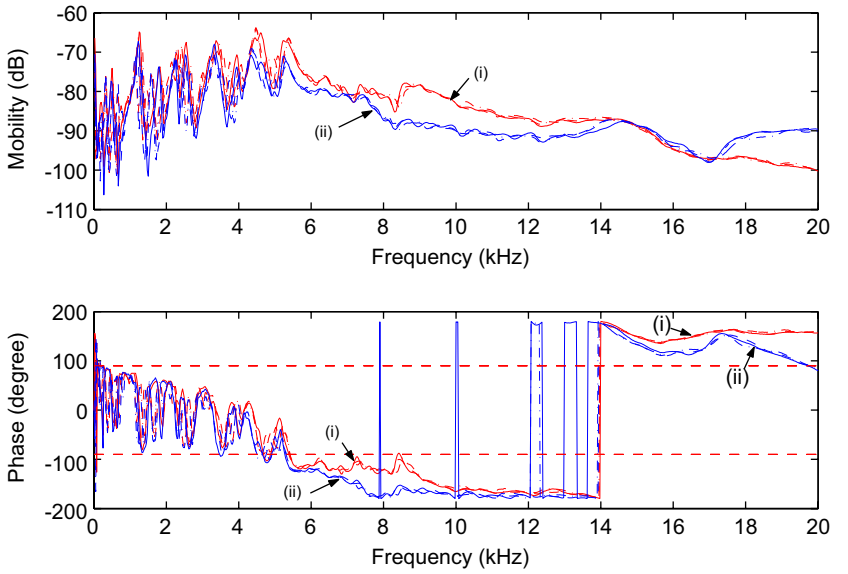

Fig. 9. Measured frequency responses for three different boundary conditions where the set of curves (i) is for honeycomb beams having an accelerometer mass of 2.5 g and (ii) is for the same beams having an accelerometer mass of 5.0 g.

actuator side. This response is depressed in the frequency range from 10 to 30 kHz due to the lumped mass. The mass, however, does not make the response roll off as much as the accelerometer located on the opposite skin of the actuator location does. Although, there is no obvious peak in the high frequencies when the accelerometer is located on the opposite side of the actuator location of the honeycomb beam, the response does roll off with the same rate of 12 dB/oct as that for the force actuation.

For the piezoelectric actuation, the response functions are again measured under different conditions, changing boundary conditions, the length of the beam and the mass of the sensor. The arrangement for clamping the beam at $0.4L$ and $0.6L$ and doubling the mass of the sensor is shown in Fig. 8. The response functions under these different conditions are shown and compared in Fig. 9. The mass of the accelerometer affects the response functions decreasing the resonance frequency, as expected, although it is not apparent. The beam length and the boundary condition do not influence the response function at high frequencies too; so the response at the high-frequency is dominated by the local dynamics of the sensor and actuator. It is concluded that the local coupling does exist between the piezoceramic actuator and the sensor, although it is highly damped.

4. Modelling of the local dynamic coupling

In this section, the local dynamic coupling is modelled as an additional single degree of freedom (sdof) system added to the dynamics of a beam. It is believed that this behaviour is caused by the locally added mass of the sensor and actuator and the local stiffness of the honeycomb structure. For the force actuation, the local parameters can be obtained from the transmissibility between both skins at the location of the actuator–sensor pair. The transmissibility, TR, can be expressed by

$$\mathrm{TR} = \frac{v_U}{v_L} = \frac{\mathrm{j}\omega c_u + k_u}{-m_u\omega^2 + \mathrm{j}\omega c_u + k_u}, \tag{11}$$

where v_U and v_L are the velocity at the sensor location and the actuator location, respectively, m_u is the mass of the sensor, 2.5 g in this case, and c_u and k_u are the local damping and stiffness to be found from the transmissibility measurement. Note that the transmissibility between both skins modelled by the sdof system does not depend on the beam's properties, its dynamics or the lumped mass at that location, but only depends on the local parameters (Fig. 10). In Fig. 11, the measured transmissibility is compared with that predicted with several damping factors. From the centre frequency of the transmissibility, we can estimate $k_u = 1.8 \times 10^6$ N/m and from its shape $\zeta_a = c_u/2\sqrt{m_u k_u} = 0.025$.

Using the model presented in Section 2, the coupled response (faint solid) of the force actuator to accelerometer on the beam is calculated and shown in Fig. 12. The geometrical data and the material properties estimated by the procedure given in Ref. [13] are listed in Table 1. The calculated and measured frequency responses are in reasonable agreement. The predicted frequency response without the coupling model is also shown in Fig. 12, which has the same behaviour as that measured using laser vibrometer. It can be seen that the local coupling leads to the phase shift at the local coupling resonance and so the unstable Nyquist loop. Hence, the feedback control system using force actuator/velocity sensor on honeycomb structures becomes only conditionally stable.

The transmissibility between both skins with the piezoceramic actuator is now measured. In this configuration, however, the skin of the honeycomb beam at the actuator location is covered by the piezoceramic so that it is impossible to measure the exact transmissibility. An approximate transmissibility is, however, obtained by measuring the velocities at the centre of the piezoactuator and the same point on the opposite skin. Fig. 13 shows the measured transmissibility (thick solid) and calculated transmissibility of the local area of the honeycomb beam excited by a piezoactuator for several damping factors, ζ_a, of 0.0125 (solid), 0.025 (dot-dashed), 0.2 (dashed), and 0.4 (dotted). The stiffness of the local area can be estimated as $k_u = 2.7 \times 10^6$ N/m from the centre frequency. This is somewhat higher than with the force actuator, presumably

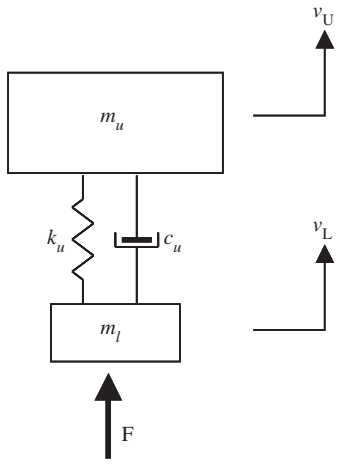

Fig. 10. Transmissibility model due to the local coupling.

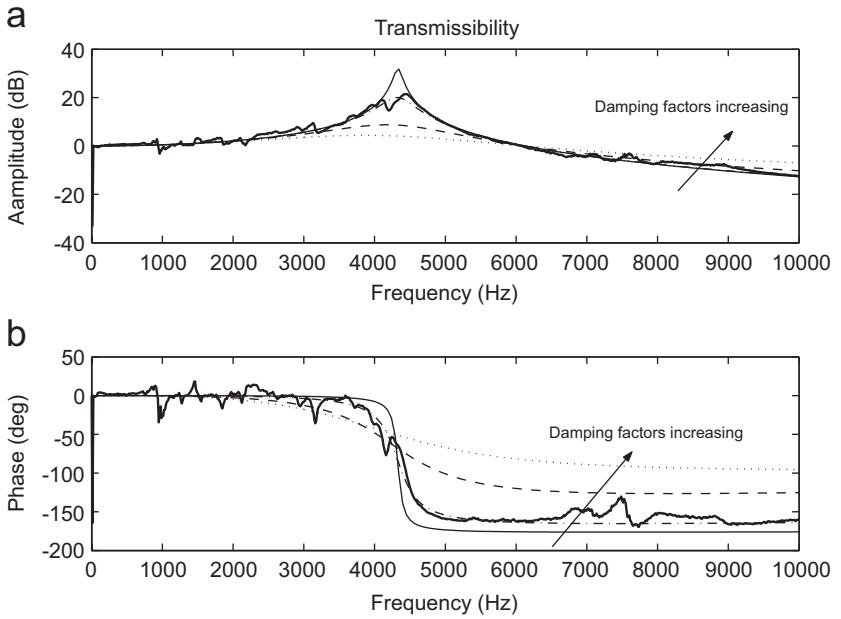

Fig. 11. Measured transmissibility (thick solid) and calculated transmissibility of the local area of the honeycomb beam excited by a force actuator for several damping factors, ζ_a, of 0.0125 (solid), 0.025 (dot-dashed), 0.2 (dashed), and 0.4 (dotted).

due to increase of the local stiffness due to the piezoceramic bonded on the local area of the honeycomb structure. The approximate damping ratio appears to be about 0.025.

The damping factor of the local area was also estimated by comparing the measured frequency response from piezoactuator to accelerometer with that predicted from this model for several damping factors. Fig. 14 shows the calculated frequency responses for several damping factors and the measured one. The predictions are in reasonable agreement with the measurements below 2 kHz if the damping ratio is assumed to be 0.2. This is somewhat higher than that measured with the laser vibrometer, presumably because of the additional shear deformation caused by the constraining effect of the accelerometer body. The difference above 2 kHz is due to the structure starting to behave as a plate. The natural frequency at which the half-wave length of the corresponding mode is less than the beam width is about 2 kHz, above which the beam responds with bending waves in the width, which causes the beam to respond with an increased level. When the beam has plate modes, the torsional moment generated by the piezoceramic actuator also couples into the plate behaviour, so that the response is increased even more. The measured response at frequencies above 5 kHz also shows that no distinct modal behaviour exists. This is because the modal density due to the shear waves becomes large enough to smooth the response due to the high modal overlapping in the real honeycomb. The predicted response could have a similar smooth frequency dependence at the high frequencies, provided that the damping factor is selected properly, although the magnitude is different. The response functions also display apparent phase shifts of two kinds; one is due to the non-collation between the sensor and the actuation which leads to the slowly shifting phase over the frequency first and then a sudden change in phase at the frequency where the half-wave length begins to be less than the distance between the sensor and actuator. This frequency is about 14 kHz in this case which is evaluated from the nth natural frequency such that $n = L/s$. This phase shift can be seen in both results around this frequency. The other phase shift which can be found at about 5 kHz is due to the local coupling. The phase shift is not as much as that shown in Fig. 12 for the force actuation. This behaviour is thought to be due to higher damping caused by the more constrained local interaction between the accelerometer and the piezoceramic actuator. The higher local damping and local stiffness lead to the coupling at higher frequency, smoothing the coupling resonance peak, and reducing the phase shift rate.

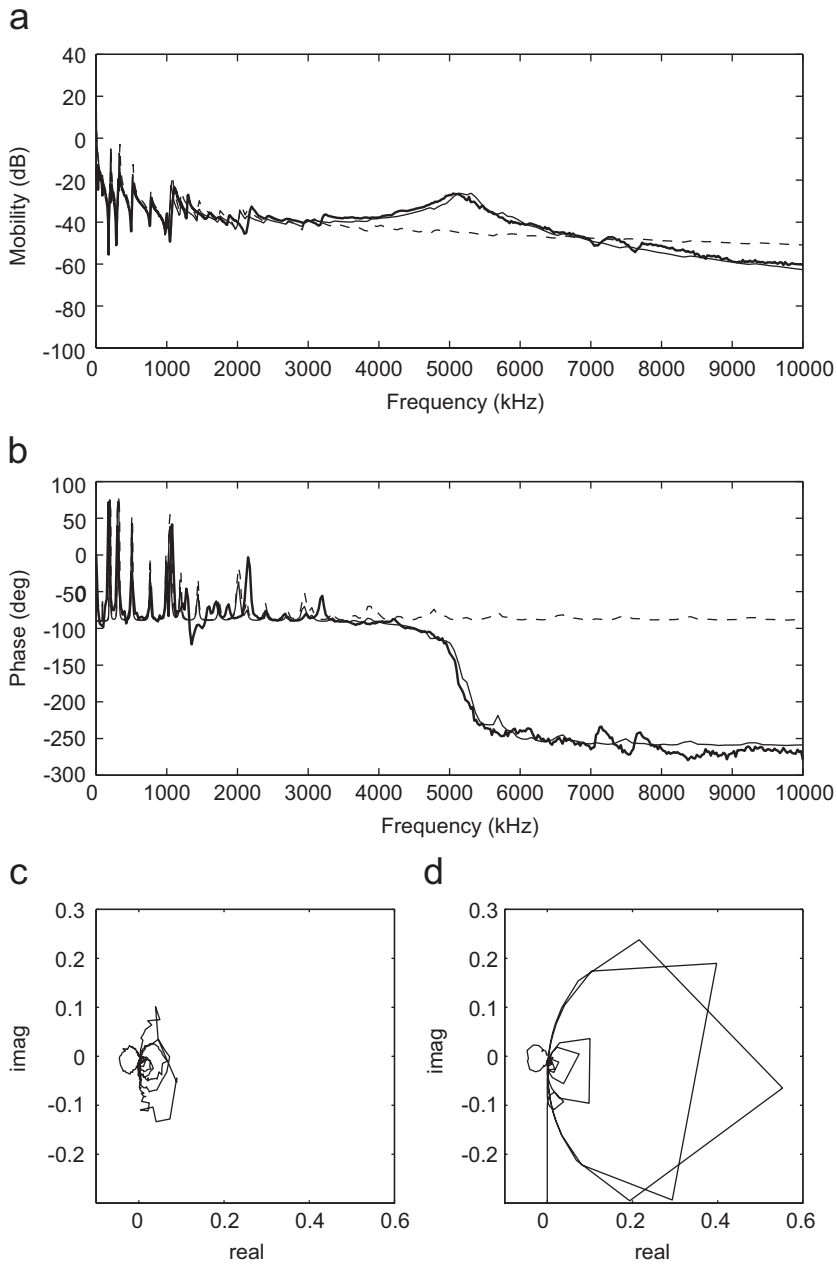

Fig. 12. Comparison of the measured mobility functions (thick solid line), with the force applied on one side and the velocity measured at the same point on the other side, with that predicted from the model with no local dynamics (dashed) and with local dynamics (solid), having $\zeta_a = 0.025$: (a) magnitude, (b) phase, (c) measured Nyquist plot and (d) predicted Nyquist plot.

5. Direct velocity feedback control with a piezoceramic actuator

In this section, a control system for honeycomb beams using a piezoceramic actuator is implemented, as shown in Fig. 15, in order to estimate the effects of the local coupling on the stability and the control performance. The honeycomb beam is supported by wire at both ends which is a mounting device having

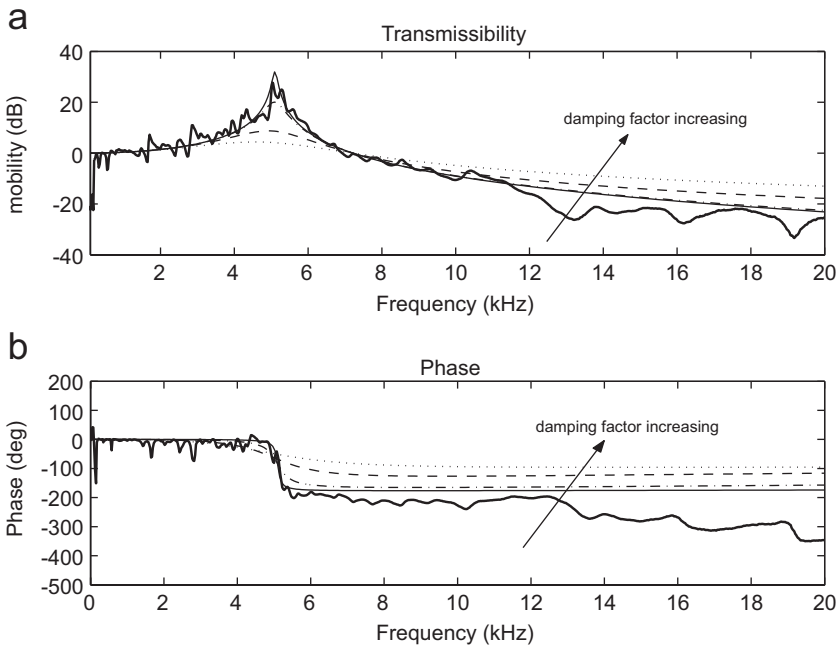

Fig. 13. Measured transmissibility (thick solid) and calculated transmissibility of the local area of the honeycomb beam excited by a piezoactuator for several damping factors, ζ_a, of 0.0125 (solid), 0.025 (dot-dashed), 0.2 (dashed), and 0.4 (dotted).

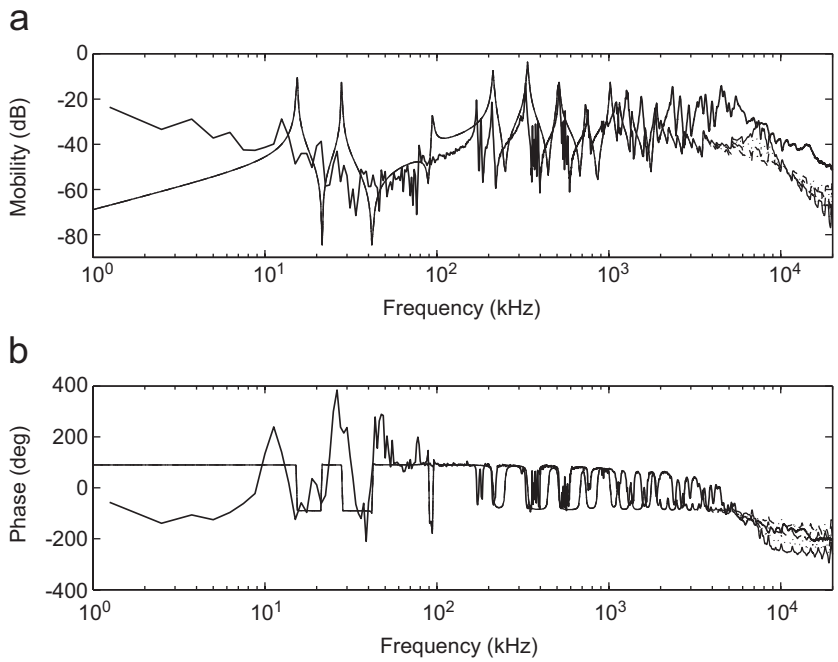

Fig. 14. Measured plant response (thick solid line) from the moment pair applied on one side to the velocity measured at the same point on the other side, and predicted response using the model with the local coupling having stiffness from transmissibility measurement and various damping factors of ζ_a, are 0.025 (solid), 0.1 (dotted), 0.2 (dashed), and 0.4 (dot-dashed).

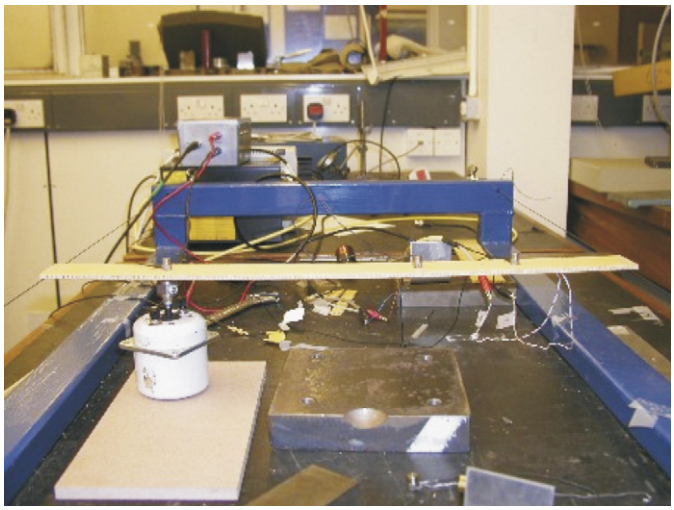

Fig. 15. Photographic view of the experiment.

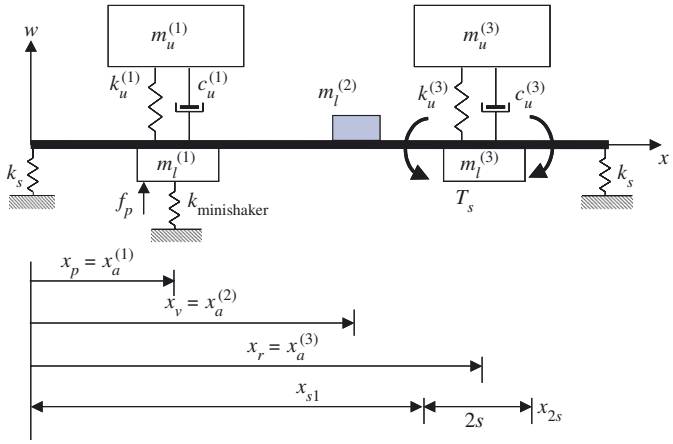

Fig. 16. Theoretical model for the honeycomb structure under the control system using a piezoceramic actuator.

vertical stiffness of about 140 N/m. The dimensions and estimated mechanical properties of the honeycomb beam are listed in Table 1. The lumped masses and the stiffness and the local coupling models are included in the theoretical model [16] shown in Fig. 16. The shaker for the primary force is modelled as a sdof mass–spring system. The parameters in the model are summarised in Table 2.

5.1. Plant response and stability

The measurement of the plant response, from piezoceramic actuator input to integrated accelerometer output, was performed as shown in Fig. 17. Several unconnected accelerometers and a shaker are present, which are used later for monitoring the performance of the control system and disturbing the beam as a primary source when measuring control performances. The plant response is measured from 0 to 20 kHz, as shown in Fig. 18, in order to characterise the stability in the high-frequency range. It can be seen that the magnitude of the plant response decays almost monotonically as the frequency increases, and its phase is shifted slowly at the same time. The decay in the magnitude and the shift in phase are caused by the local coupling of the actuator–sensor pair with the honeycomb structure. This behaviour is represented as a helical curve approaching to the origin, in the complex plane. The response within a unit circle about the point

Table 2
Parameters in Figs. 17(b) and 21(b)

Notation	Unit	Value	Description
L	m	0.51	Length of the beam
x_p	m	$0.2L$	Location of primary source
x_s	m	$0.8L$	Location of piezoceramic actuator
x_v	m	$0.6L$	Location of monitoring sensor
x_a	m	x_s	Location of feedback sensor
x_m	m	0.005	Location of mount
$2s$	mm	13	Length of piezoceramic actuator
x_{s1}	m	$x_s - s$	Location of moment 1
x_{s2}	m	$x_s + s$	Location of moment 2
k_s	N/m	143.5	Stiffness of mount
$k_{\text{minishaker}}$	N/m	3150	Stiffness of shaker
$m_u^{(1)}$	kg	0.0025	Mass of accelerometer
$k_u^{(1)}$	N/m	1.85×10^6	Local stiffness of the honeycomb
$c_u^{(1)}$	N s/m	$0.025 \times 2\sqrt{m_u^{(1)} k_u^{(1)}}$	Local damping of the honeycomb
$m_u^{(3)}$	kg	0.0025	Mass of accelerometer
$k_u^{(3)}$	N/m	2.42×10^6	Local stiffness of the honeycomb
$c_u^{(3)}$	N s/m	$0.2 \times 2\sqrt{m_u^{(2)} k_u^{(2)}}$	Local damping of the honeycomb
$m_l^{(1)}$	kg	$0.0025 + 0.0067$	Mass of moving coil in minishaker and accelerometer
$m_l^{(2)}$	kg	0.0025	Mass of accelerometer
$m_l^{(3)}$	kg	0.0125	Mass of piezoceramic actuator
f_p	N	NA	Primary force
T_s	N m	NA	Secondary moment pair
v_r	m/s	NA	Feedback velocity

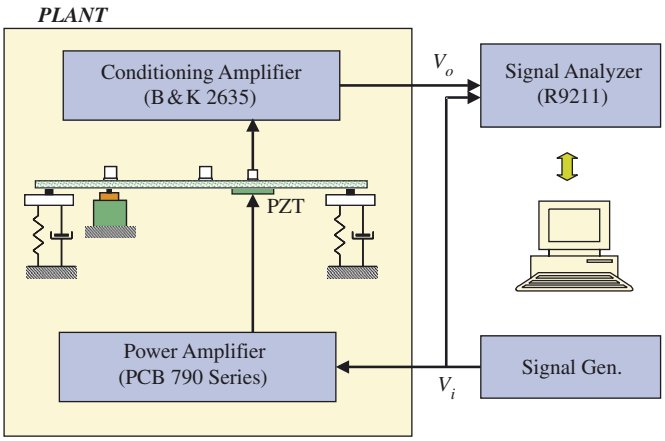

Fig. 17. Schematic diagram for the measurement of the plant response of the control system using a piezoceramic actuator and its corresponding theoretical model.

$(-1, j0)$, shown dashed in Fig. 18, leads to the enhancement when the feedback control is active [17]. The first frequency crossing this unit circle occurs at 5.5 kHz in Fig. 18. When activated feedback control, this frequency varies with the feedback gain. Fig. 19 shows the predicted plant response which is seen to predict the measured results reasonably. It is interesting in this stage to show the plant response for the normal solid structure when using a piezoceramic actuator. Fig. 20 shows the plant response measured for a 2 mm thick

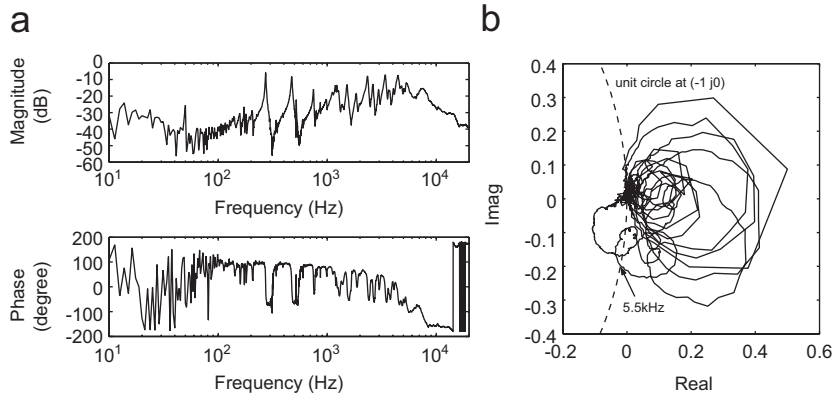

Fig. 18. Measured plant response of the feedback control system for a honeycomb beam using a piezoceramic actuator in the frequency range of 0–20 kHz: (a) Bode diagram and (b) Nyquist plot.

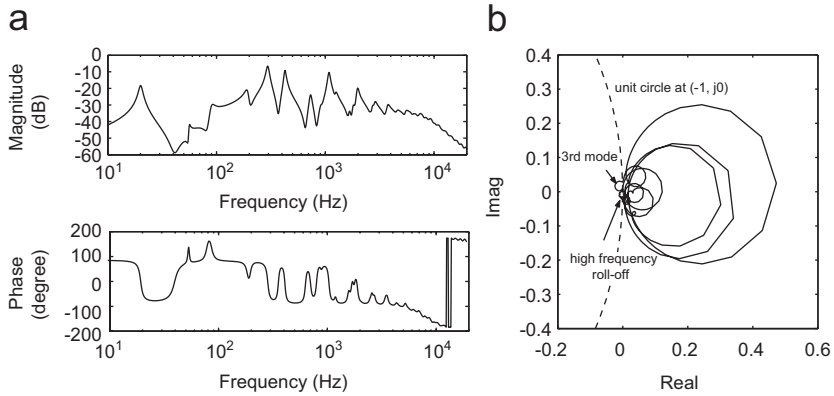

Fig. 19. Predicted plant response of the feedback control system for a honeycomb beam using a piezoceramic actuator in the frequency range of 0–20 kHz: (a) Bode diagram and (b) Nyquist plot.

aluminium beam of the same size as the honeycomb beam used in this study excited by the piezoceramic actuator at the same location. It can be seen that the magnitude of the plant response in the high-frequency range keeps at a high level, since the piezoceramic actuator effectively couple into high-frequency modes, while the phase is slowly shifted as the frequency increases because of the non-collocation effect of the actuator–sensor pair at high frequencies. The larger loops on the left-hand side of the Nyquist plot lead to much poorer performance than on the honeycomb structure for a given gain margin. It is suggested for the aluminium beam to implement a low-pass filter to enforce a high-frequency roll-off, but this can introduce destabilising phase shifts.

5.2. Control performance

The control system for a honeycomb structure using a piezoceramic actuator is evaluated by measuring the velocities along the beam at three points as shown in Figs. 15 and 21. A mini-shaker, LDS V101, is used to generate disturbances on the honeycomb beam and the piezoceramic actuator is mounted at $0.8L$ to achieve control. The control actuator is driven by the signal from the accelerometer, integrated by the built-in integrator in the conditioning amplifier. The feedback gain can be adjusted by the transducer's sensitivity control knob and mV/UNIT OUT Switch [18]. The transducer's sensitivity control allows the feedback gain to be adjusted with a fine increment. The feedback gain is inversely proportional to the set value of the

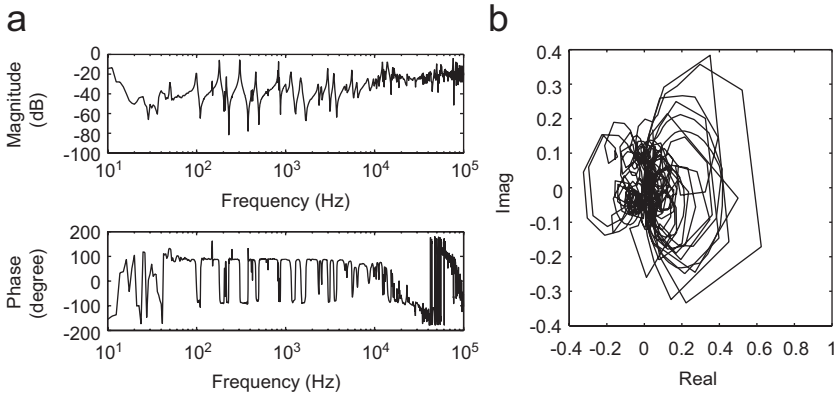

Fig. 20. Measured plant response of the feedback control system for an aluminium beam, having the thickness of 2 mm, the length of 510 mm and the width of 40 mm, using a piezoceramic actuator in the frequency range of 0–100 kHz: (a) Bode diagram and (b) Nyquist plot.

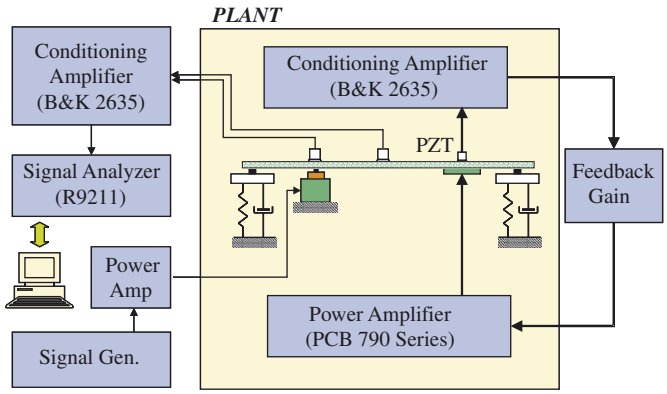

Fig. 21. Schematic diagram for the measurement of the control performance of the control system using a piezoceramic actuator and its corresponding theoretical model.

transducer's sensitivity control knob, S_{set}. The measurements are performed with nine feedback gains and without control, and at three points on the beam, at the primary source position ($x = 0.2L$), at the secondary source location ($x = 0.8L$) and in between at $x = 0.6L$. The measurement were carried out for the frequency range of 0~10 kHz. The feedback gains used in the simulation are 200, 400 and 1000.

Fig. 22 shows the measured and predicted velocity levels at the primary source location ($x = 0.2L$) and show that very little attenuation is measured as predicted at this position. The differences between measurement and simulation below 1 kHz are due to the dynamics of the force actuator. Since the dynamics of the beam at $x = 0.2L$ is mainly governed by the local dynamics of the force actuator, and the control actuator is far from this monitoring sensor, the velocity is not significantly reduced. The broad peak in the response at 4.5 kHz in Fig. 22, at the shaker location, is due to the local coupling of the sensor/primary force actuator as measured in the previous section.

Fig. 23 shows the measured and predicted velocity levels at $x = 0.6L$. It can be seen that the control system reduces the vibration level at this point between the primary actuator and control position by a maximum of about 15 dB at 500 Hz. There is, however, no reduction at around 1 kHz because the response is strongly coupled with the dynamics of the mini-shaker at this frequency.

Finally, Fig. 24 shows the measured and predicted velocity levels at the secondary source location ($x = 0.8L$). The feedback controller is much more effective here with all resonance peaks being controlled

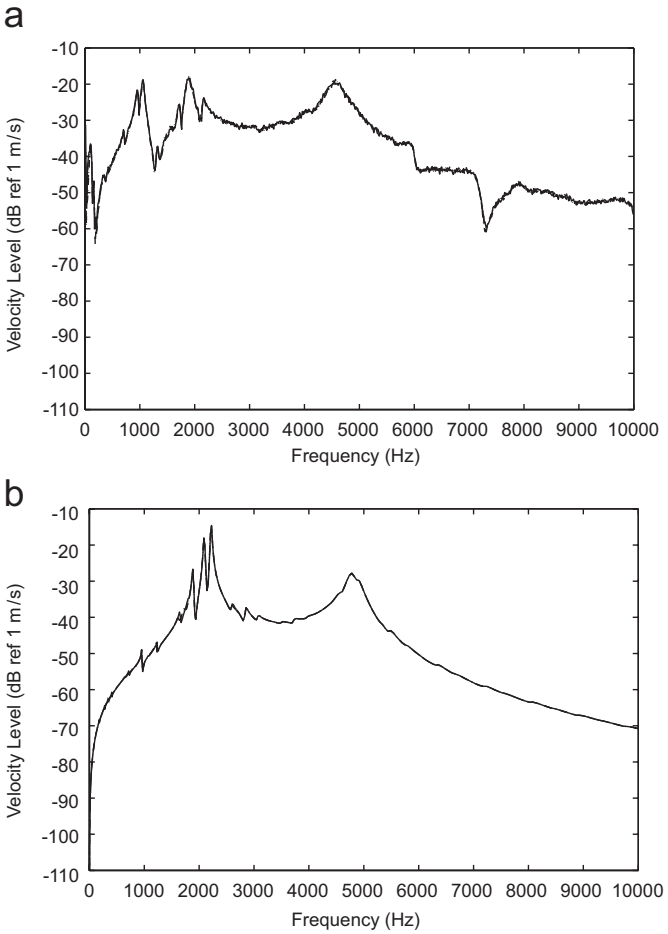

Fig. 22. Velocity level at primary driving position, of the beam disturbed by the primary driving force at $x = 0.2L$ (solid), and subjected to the feedback control with gains of 200 (dotted), 400 (dashed) and 1000 (dot-dashed): (a) measured and (b) predicted.

above 200 Hz. The control system enhances the velocity at some frequencies and reduces it at others. For instance, the velocity is enhanced at the frequencies between 6.5 and 8 kHz at the control location, as the feedback gain increases, as expected from the Nyquist plot. Below 6.5 kHz, however, significant reductions in vibration, about 20 dB, are measured at the control location.

It is clear from Figs. 22 and 23, however, that these high frequency reductions are rather local. The advantage of the local coupling behaviour on the honeycomb beam is that it makes the feedback loop using a piezoceramic actuator and accelerometer more stable. The disadvantage appears to be that it is difficult to achieve global control of the vibration on the beam, although this may be due to the presence of the heavy primary shaker in these experiments.

6. Conclusion

This paper has been concerned with local coupling between closely located actuators and sensors on honeycomb structures. From the measurement of the frequency response using an accelerometer located on the one of the skins of the honeycomb beam and a force actuator located on the other skin, a strong coupling resonance was discovered. It was found that the coupling behaviour can be modelled using a single-degree-of-freedom mass–spring–damper system whose parameters—local stiffness and damping factor—can be

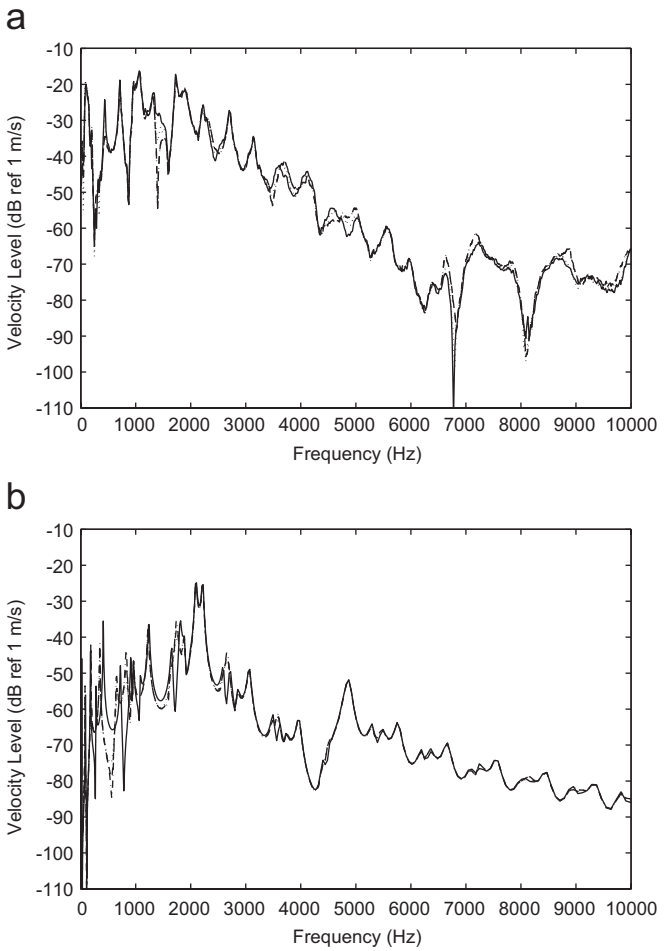

Fig. 23. Velocity level at $x = 0.6L$ of the beam disturbed by the primary driving force at $x = 0.2L$ (solid), and subjected to the feedback control with gains of 200 (dotted), 400 (dashed) and 1000 (dot-dashed): (a) measured and (b) predicted.

evaluated from the measured transmissibility. The prediction model including the local dynamics is validated by comparing the measured frequency response with the predicted one including a local coupling. Another series of experiments and simulations were performed to define the local coupling when the honeycomb beam excited by a piezoceramic actuator. The local stiffness was reasonably approximated using the measured transmissibility, but the local damping factor somewhat higher than that estimated from transmissibility due to local interaction between the beam, the piezoceramic actuator and the accelerometer body. The high-frequency roll-off provided by this coupling provides an inherent stabilising mechanism in honeycomb structures subjected to the direct velocity feedback control system using piezoactuator-velocity sensor pair.

A control system was implemented for a resiliently mounted honeycomb beams using a piezoceramic actuator. The calculated plant response compares reasonably well with that measured. The feedback control system is conditionally stable, but it has a high gain margin compared to a solid beam. The high gain margin results from the existence of the local dynamics which leads to a slowly shifting phase and high-frequency roll-off. It is noted, however, that the local dynamics causes the controlled response to be enhanced above the coupling frequency. The control performance is then evaluated in terms of the velocity levels at three points on the beam; at the primary source location ($0.2L$), at the secondary source location ($0.8L$), and at $0.6L$. A large reduction in the velocity at the secondary source location can be achieved, although having enhancement at

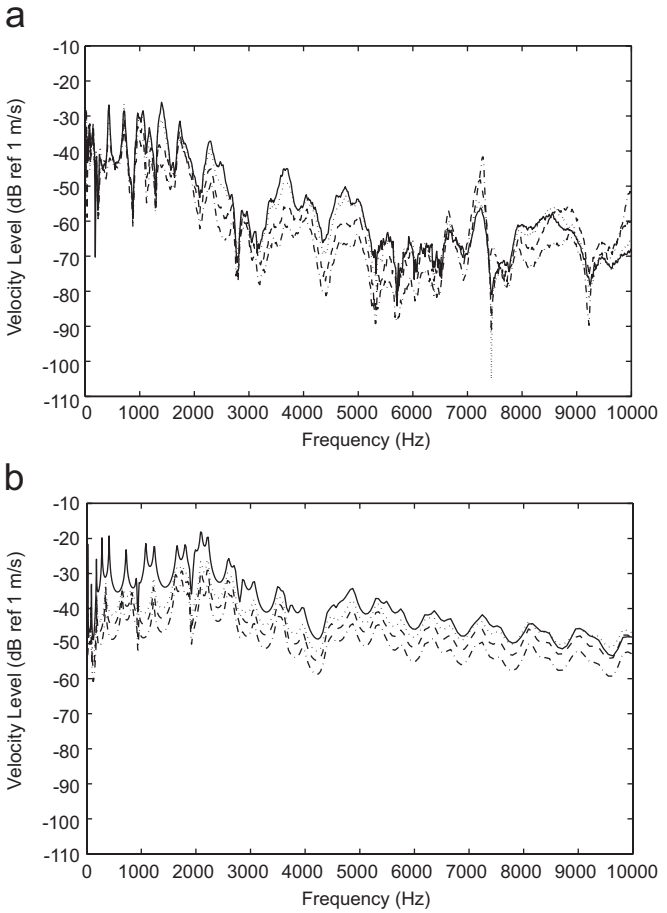

Fig. 24. Velocity level at the control location, $x = 0.8L$, of the beam disturbed by the primary driving force at $x = 0.2L$ (solid), and subjected to the feedback control with gains of 200 (dotted), 400 (dashed) and 1000 (dot-dashed): (a) measured and (b) predicted.

high frequencies. A smaller reduction is obtained away from the secondary source and hardly any reduction is obtained at the primary source location.

Appendix A. Free vibration of a resiliently supported beam

The free vibration of honeycomb beams can be assumed to be

$$W(x) = c_1 e^{-j\alpha x} + c_2 e^{j\alpha x} + c_3 e^{-\beta x} + c_4 e^{\beta x}. \tag{A.1}$$

Applying the boundary conditions to Eq. (A.1) yields the eigenvalue problem so that the natural frequencies and mode shapes can be obtained theoretically. However, as demonstrated in Ref. [19], it is impossible to obtain the higher order mode shapes numerically due to divergence of the terms c_3, c_4 and $e^{\beta x}$ which include $e^{\beta L}$. To avoid this divergence, the dual coordinate system technique [19] is used although there is a problem at higher values of β.

In this paper, more complete wave approach is introduced. The solution can be rewritten as the superposition of the wave components at x as

$$\begin{aligned} W(x) &= a_F^+ e^{-j\alpha x} + a_F^- e^{j\alpha x} + a_N^+ e^{-\beta x} + a_N^- e^{\beta x} \\ &= [1 \;\; 1]\mathbf{P}(x)\mathbf{a}^+ + [1 \;\; 1]\mathbf{P}(-x)\mathbf{a}^-, \end{aligned} \tag{A.2}$$

where the (2×2) matrix, $\mathbf{P}(x)$, called the *propagation matrix*, is of the form

$$\mathbf{P}(x) = \begin{bmatrix} e^{-j\alpha x} & 0 \\ 0 & e^{-\beta x} \end{bmatrix}, \tag{A.3}$$

for which $\mathbf{P}(-x) = \mathbf{P}(x)^{-1}$, and the wave components, $\mathbf{a}^+$ and $\mathbf{a}^-$ shown in Fig. A.1, are given by

$$\mathbf{a}^+ = \begin{Bmatrix} a_F^+ \\ a_N^+ \end{Bmatrix} \quad \text{and} \quad \mathbf{a}^- = \begin{Bmatrix} a_F^- \\ a_N^- \end{Bmatrix}. \tag{A.4}$$

It is noted that Eq. (A.2) is the same form as Eq. (A.1) so that the numerical divergence should occur. This is mainly caused by the existence of the inverse of the propagation matrix in the eigenvalue problem obtained after applying the boundary conditions to Eq. (A.2), but

$$\mathbf{a}^- = \mathbf{P}(L)\mathbf{b}^-, \quad \mathbf{a}^- = \mathbf{R}_0\mathbf{a}^+, \quad \mathbf{b}^+ = \mathbf{P}(L)\mathbf{a}^+ \quad \text{and} \quad \mathbf{b}^- = \mathbf{R}_L\mathbf{b}^+, \tag{A.5}$$

where $\mathbf{b}^+$, and $\mathbf{b}^-$ are the wave components at $x = L$, as shown in Fig. A.1, and $\mathbf{R}_0$ and $\mathbf{R}_L$ denote the *reflection coefficient matrices* at $x = 0$ and L, respectively.

From Eq. (A.5), we can obtain

$$\mathbf{a}^- = \mathbf{P}(L)\mathbf{R}_L\mathbf{P}(L)\mathbf{a}^+. \tag{A.6}$$

Substituting Eq. (A.6) into Eq. (A.2), the solution can be written in terms of $\mathbf{a}^+$ having a well-conditioned propagation matrix, $\mathbf{P}(L - x)$ as

$$\begin{aligned} W(x) &= [1 \;\; 1]\mathbf{P}(x)\mathbf{a}^+ + [1 \;\; 1]\mathbf{P}(L-x)\mathbf{R}_L\mathbf{P}(L)\mathbf{a}^+ \\ &= [1 \;\; 1](\mathbf{P}(x) + \mathbf{P}(L-x)\mathbf{R}_L\mathbf{P}(L))\mathbf{a}^+. \end{aligned} \tag{A.7}$$

The solution for rotational angle, Φ_x, can be obtained by substituting Eq. (A.7) into the homogeneous equation of Eq. (1). The distribution of Φ_x becomes

$$\Phi_x(x) = [jC_P \;\; C_N](\mathbf{P}(x) + \mathbf{P}(L-x)\mathbf{R}_L\mathbf{P}(L))\mathbf{a}^+, \tag{A.8}$$

where

$$C_P = \left(\alpha - \frac{I_0\omega^2}{KA_{55}\alpha}\right), \tag{A.9}$$

$$C_N = \left(\beta + \frac{I_0\omega^2}{KA_{55}\beta}\right). \tag{A.10}$$

The eigenvalue problem can be found by considering the boundary characteristics as denoted in Eq. (A.5). Expressing it in terms of only $\mathbf{a}^+$, the eigenvalue problem is of the form

$$(\mathbf{I} - \mathbf{R}_0\mathbf{P}(L)\mathbf{R}_L\mathbf{P}(L))\mathbf{a}^+ = \mathbf{0}. \tag{A.11}$$

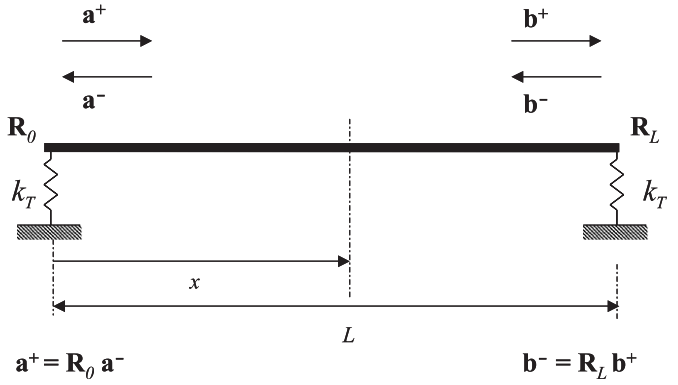

Fig. A.1. Wave components on beams and boundary conditions.

For non-trivial solutions of $\mathbf{a}^+$,

$$|\mathbf{I} - \mathbf{R}_0\mathbf{P}(L)\mathbf{R}_L\mathbf{P}(L)| = 0, \tag{A.12}$$

so that a set of the wavenumbers can be obtained. The set of the natural frequencies can then be determined using the dispersion equation as

$$\begin{aligned} k_x^2 &= \frac{1}{2D_{11}}\left\{ -\omega^2\left(I_2 + \frac{I_0 D_{11}}{KA_{55}}\right) \pm \sqrt{\omega^4\left(I_2 + \frac{I_0 D_{11}}{KA_{55}}\right)^2 + 4D_{11}\left(1 - \frac{\omega^2 I_2}{KA_{55}}\right)I_0\omega^2}\right\} \\ &= \frac{1}{2D_{11}}\left\{ -\omega^2\left(I_2 + \frac{I_0 D_{11}}{KA_{55}}\right) \pm \sqrt{\omega^4\left(I_2 - \frac{I_0 I_2}{KA_{55}}\right)^2 + 4D_{11}I_0\omega^2}\right\}. \end{aligned} \tag{A.13}$$

The reflection matrices at both ends, $\mathbf{R}_0$ and $\mathbf{R}_L$, can be evaluated considering the incident wave to the boundary and the reflected wave from it as shown in Fig. A.1. Substituting Eqs. (A.7) and (A.8) into Eq. (7), the reflection matrix at $x = 0$, $\mathbf{R}_0$, becomes

$$\mathbf{R}_0 = \begin{bmatrix} -\mathrm{j}C_P + \mathrm{j}\alpha + \tilde{k}_T & -C_N + \beta + \tilde{k}_T \\ \alpha C_P & -\beta C_N \end{bmatrix}^{-1} \begin{bmatrix} -\mathrm{j}C_P + \mathrm{j}\alpha - \tilde{k}_T & -C_N + \beta - \tilde{k}_T \\ -\alpha C_P & \beta C_N \end{bmatrix}, \tag{A.14}$$

where $\tilde{k}_T = k_T/KA_{55}$. Assuming that the spring constants at both ends are the same, the reflection matrices at both ends are the same so that $\mathbf{R}_L = \mathbf{R}_0 = \mathbf{R}$. Substituting the reflection matrix, $\mathbf{R}$, into Eqs. (A.7) and (A.8), the mode shape function can be obtained. Fig. A.2(a) and (b) show the natural modes for the transverse displacement and the angle of the cross-sectional area, respectively, which are well defined up to 20th order using this method.

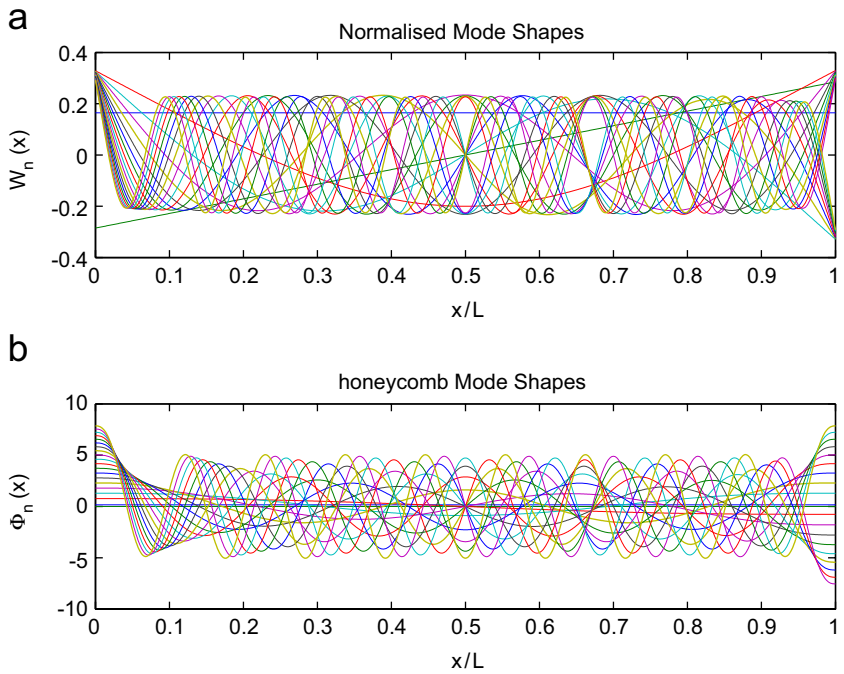

Fig. A.2. First 20 mode shape functions of a free–free honeycomb beam: (a) transverse mode, $W_n(x)$ and (b) rotational mode, $\Phi_n(x)$.

References

[1] A. Preumont, *Vibration Control of Active Structures*, Kluwer Academic, Dordrecht, 1997.

[2] S.J. Elliott, P. Gardonio, T.C. Sors, M. Brennan, Active vibroacoustic control with multiple local feedback loops, *Journal of Acoustical Society of America* (2002) 908–915.

[3] P. Gardonio, E. Bianchi, S.J. Elliott, Smart panel with multiple decentralized units for the control of sound transmission, part i: theoretical predictions, *Journal of Sound and Vibration* 274 (2004) 163–192.

[4] P. Gardonio, E. Bianchi, S.J. Elliott, Smart panel with multiple decentralized units for the control of sound transmission, part ii: design of decentralized control units, *Journal of Sound and Vibration* 274 (2004) 193–213.

[5] M. Serrand, *Direct Velocity Feedback Control of Equipment Vibration*, MPhil Thesis, University of Southampton, 2000.

[6] M. Ruzzene, Vibration and sound radiation of sandwich beams with honeycomb truss core, *Journal of Sound and Vibration* 277 (2004) 741–763.

[7] M. El-Raheb, Frequency response of a two-dimensional trusslike periodic panel, *Journal of Acoustical Society of America* (1996) 3457–3465.

[8] M. El-Raheb, P. Wagner, Transmission of sound across a trusslike periodic panel; 2-d analysis, *Journal of Acoustical Society of America* (1997) 2176–2183.

[9] J.N. Reddy, *Mechanics of Laminated Composite Plates*, CRC Press Inc., Boca Raton, FL, 1996.

[10] T.S. Lok, Q.H. Cheng, Free vibration of clamped orthotropic sandwich panel, *Journal of Sound and Vibration* (1999) 311–327.

[11] A.K. Noor, Continuum modeling for repeative lattice structures, *Applied Mechanics Reviews* 41 (7) (1988) 285–296.

[12] U. Lee, Equivalent continuum models of large platelike lattice structures, *International Journal of Solids and Structures* 31 (4) (1994) 457–467.

[13] E. Nilsson, A.C. Nilsson, Prediction and measurement of some dynamic properties of sandwich structures with honeycomb and foam cores, *Journal of Sound and Vibration* 251 (2002) 409–430.

[14] J. Soovere, *Dynamic Response of Acoustically Excited Stiffened Composite Honeycomb Panels*, PhD Thesis, University of Southampton, 1984.

[15] E.B. Magrab, *Vibrations of Elastic Structural Members*, Sijthoff & Noordhoff International Publishers B.V., Alphen aan den Rijn, 1979.

[16] C. Hong, *Active Control of a Resiliently-mounted Flexible Structures*, PhD Thesis, Institute of Sound and Vibration, University of Southampton, 2005.

[17] G.F. Franklin, J.D. Powell, A. Emami-Naeini, *Feedback Control of Dynamic Systems*, second ed., Addison-Wesley Publishing Company, Inc., Reading, MA, 1991.

[18] *Instruction Manual*, *Charge Amplifier Type 2635*, Bruel & Kaer, Wallingford, 1991.

[19] C. Hong, S.J. Elliott, Active control of resiliently-mounted beams with a moment pair, *Smart Materials and Structures* 14 (2005) 727–738.